




Interaction between droplets and co-flow interface in a microchannel: Droplet migration and interfacial deformation

S. Hazra ¹, L. Malik ¹, S. K. Mitra,³ and A. K. Sen ^{1,2,*}

¹*Fluid Systems Laboratory, Dept. of Mechanical Engineering, Indian Institute of Technology Madras, Chennai-600036, India*

²*Micro Nano Bio-Fluidics Group, Indian Institute of Technology Madras, Chennai-600036, Tamilnadu, India*

³*Waterloo Institute for Nanotechnology, Dept. of Mechanical & Mechatronics Engineering, University of Waterloo, Ontario N2L 3G1, Canada*



(Received 21 January 2022; accepted 26 April 2022; published 16 May 2022)

We report hydrodynamic interaction between droplets and the interface of a pair of co-flowing immiscible streams in a microchannel revealing droplet migration and interfacial deformation. We find small droplets of confinement ratio, i.e., ratio of drop size to the suspending stream width, $\beta < 1$, exhibit lateral migration—while smaller droplets of $\beta < 0.5$ migrate towards the co-flow interface, unexpectedly larger droplets of $0.5 < \beta < 1$ drift away from the interface. The size-based contrasting migration behavior is attributed to the interplay between the hitherto unexplored wall-directed negative lift force and the well-established center-directed noninertial lift force. We also find large droplets of $\beta > 1$ cause deformation waves in an initially stable and flat interface that propagate downstream akin to traveling peristaltic waves. Numerical simulations reveal that interfacial deformation is a consequence of the distinctive pressure jumps across the co-flow interface at the upstream and downstream of a droplet. Our study reveals the amplitude of the deformation wave associated with a droplet grows spatially downstream but remains the same for a train of droplets crossing a fixed location, indicating convective instability. The effects of co-flow interfacial tension, viscosity contrast, confinement ratio, and droplet spacing on the deformation wave amplitude and its variation along the flow direction are studied. The experimental results are verified using a simple theoretical model. Our study presents an unexplored droplet-driven interfacial deformation wave that may find relevance in droplet microfluidics.

DOI: [10.1103/PhysRevFluids.7.054201](https://doi.org/10.1103/PhysRevFluids.7.054201)

I. INTRODUCTION

Interfacial instability in stratified multiphase flows has intrigued researchers for over a century [1–3]. The different types of interfacial instabilities have been delineated according to their mechanism as Rayleigh-Plateau (RP) instability [3], Kelvin-Helmholtz (KH) instability [4], Rayleigh-Taylor (RT) instability [5,6], and Saffman-Taylor (ST) instability [7]. RP instability is governed by the competition between capillary and viscous effects whereas KH instability originates from a large velocity difference between fluid layers across an interface. RT instability is observed due to density contrast between fluid layers whereas ST instability is attributed to the entrainment of low viscous fluid in a high viscous fluid. Further, interfacial instabilities have been categorized based on the propagation mode as absolute instability wherein amplitude increases exponentially and

*Corresponding author: ashis@iitm.ac.in

disturbance propagates both upstream and downstream or convective, where instability propagates only downstream [8].

A comprehensive review [9] highlights the instability in multiphase systems in shear flow [10–14], Couette-Poiseuille flow [15–21], or core-annular co-flow [22–33] configurations. It is found that an otherwise stable single-phase Couette or Poiseuille flow, irrespective of Reynolds number, becomes unstable once viscosity stratification is introduced [34]. Long- and short-wave instability were identified for wavelengths greater and smaller than fluid layer thickness [12]. Stratified simple shear flows in bounded configuration become unstable to long waves for a wide range of Reynolds numbers [34]. On the contrary, flows become unstable to short waves in unbounded Couette flows [11]. Interfacial tension was found to have a stabilizing effect for all wave numbers while density stratification has a stabilizing or destabilizing role based on the fluid configuration [11]. Stability of semibounded Couette flow due to the viscous boundary layer at the walls [10] was studied which showed that higher viscosity of the unbounded fluid renders unstable flow. Also, with a thin viscous layer near the wall, the semibounded flow is proven to be unstable to long waves [33] while gravity has a stabilizing effect. The growth rate of disturbance for semibounded flows is found to be higher compared to the bounded one [34], revealing the possible effect of wall confinement on dampening the instability.

In the Poiseuille flow of immiscible fluids, the onset of interfacial waves in the low viscous fluid is marked by a transition to turbulence which gets amplified in a higher Reynolds number regime resulting in bulk mode instability [17]. A high value of interfacial tension (IFT) has a stabilizing effect and dampens instability below a critical Reynolds number [16]. Further, numerical investigation reaffirmed that IFT would stabilize the short-wave instability while gravity dampens the long-wave instability [21]. A subsequent experimental study demonstrated interfacial instability with low interfacial tension fluids even at low Reynold numbers and decay of growth rate with increasing IFT [35]. In core-annular flow, low-viscosity fluid at the center destabilizes the flow due to long waves [26,31] which decreases with decreasing density contrast but increases with the inclusion of IFT. In density-matched stratified systems, with the annular fluid less viscous, flow can be unstable to long-wave while short-wave instability is dampened by IFT [26]. Subsequent studies also noted the destabilizing effect of IFT [23,24] along with stabilizing effect of viscosity stratification [24]. Both planar and annular flow was found to be unstable in the presence of insoluble surfactant at the interface [28,32].

Interfacial instability in co-flow has been widely explored for microfluidic droplet generation by the virtue of transition from convective to absolute instability [22,25,36]. Large viscosity difference has been exploited to achieve wave breakup and ligament formation in parallel co-flow [37]. Further, parallel co-flows have been employed for the passive transport of microparticles and droplets, droplet splitting, particle encapsulation, size, and viscosity-based droplet sorting [38–42]. Aqueous two-phase systems have been employed for surface energy-based microparticle and cell partitioning [43,44] and hydrodynamic lift-induced cell sorting [45] across the interface. In recent years, co-flow of Newtonian-viscoelastic fluids has been employed for on-chip microparticle and cell washing and sorting [46,47]. The relevant parameters in a co-flow system are the interfacial tension, viscosities, and flow rates of the phases. The establishment of a stable co-flow system will require that the capillary numbers of the co-flowing phases be matched [48]. Similarly, the widths of the streams in a co-flow system depend on the viscosities and flow rates of the streams and can be suitably controlled by adjusting the flow rates of the co-flowing streams.

Despite the above developments in co-flow systems, the hydrodynamic interaction of droplets with co-flow interfaces has not received much attention. Moreover, the lateral migration behavior of droplets arising from the existence of an interface and interfacial deformation owing to the presence of droplets in the absence of interfacial migration of droplets remains unexplored. Literature notes viscosity and density stratification, velocity contrast, and inertia as the triggering factors for interfacial instability while portraying an inconclusive picture regarding stabilizing or destabilizing effect of viscosity contrast and IFT [9]. Further, the literature suggests that an object translating parallel to a soft membrane [49] or fluid-fluid interface [50,51] experiences an outward lift, due to

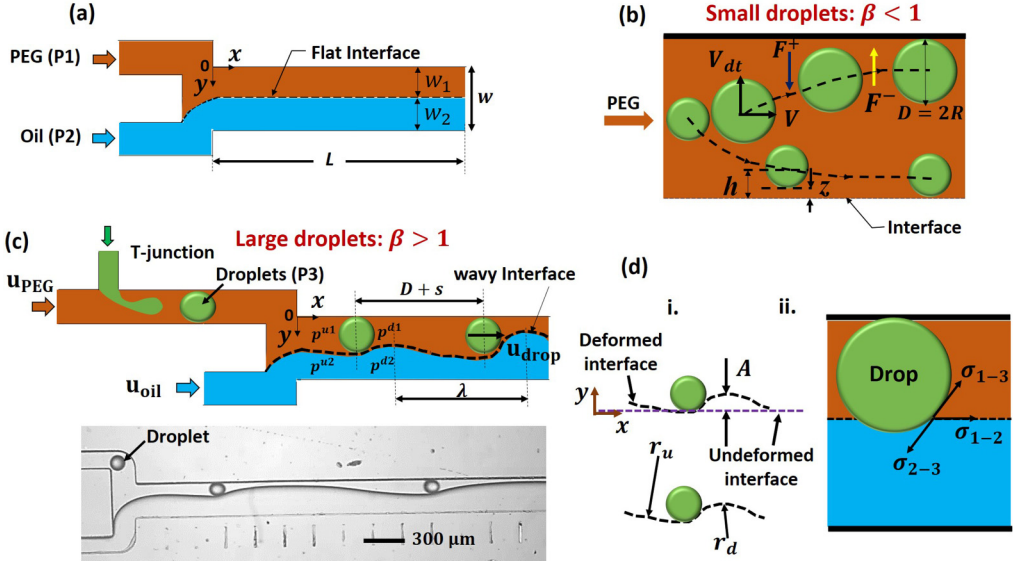


FIG. 1. Schematic showing (a) stable co-flow system between two immiscible phases, P1 and P2, flowing along a microchannel, (b) lateral migration of small droplets of size ratio $\beta = (D/W_1) < 1$ due to non inertial lift (NIL) and negative lift (NL) forces, (c) deformation of the co-flow interface in presence of larger droplets, $\beta > 1$, in P1. Experimental image showing the deformation of the PEG (flow rate $1 \mu\text{l}/\text{min}$)-SiO-100 (flow rate $10 \mu\text{l}/\text{min}$) interface due to the presence of castor oil droplets (flow rate $1 \mu\text{l}/\text{min}$). (d)-i Zoomed view of interfacial deformation for $\beta > 1$, (d)-ii Interfacial tensions at the three-phase contact line formed by the droplet in contact with co-flow interface.

which it drifts away from the interface. Evidently, the emergence of such a force comes in stark contrast to what is reported in literature [39] and will affect their dynamics. This force is strongly size sensitive, thereby allowing smaller objects to remain closer to the interface, pushing the larger objects away from the interface.

Here, we experimentally study the migration behavior of droplets and droplet-induced interfacial instability in a microfluidic co-flow system in the absence of interfacial migration. We perform experiments with droplets having a confinement ratio, i.e., droplet diameter to suspending stream width ratio, $\beta < 1$, to demonstrate the existence of an outward lift force. This negative lift force is directed opposite to the well-known noninertial lift force and controls lateral migration of droplets—an effect that is not revealed in earlier droplet—interface studies. We observe interfacial instability for larger droplets with $\beta \geq 1$ owing to a strong interaction between the droplet and interface. The effect of viscosity contrast, IFT, droplet size ratio, and spacing on the interfacial deformation is studied in terms of the spatial and temporal variation of the amplitude. We also employ a simple analytical model and numerical simulations to interpret and explain our experimental findings.

II. PROBLEM DESCRIPTION AND THEORETICAL BACKGROUND

A schematic of the stable co-flow system used for studying lateral migration of droplets and droplet-induced interfacial deformation is depicted in Fig. 1(a). Two immiscible streams, comprising a first continuous phase (P1) of width W_1 and a second continuous phase (P2), are used to establish a stable co-flow with a flat interface. Droplets of a discrete phase (P3) which is immiscible with P1 and P2 phases, of diameter D are introduced into P1. The lateral migration behavior of small droplets of size ratio $\beta = (D/W_1) < 1$ and deformation of the co-flow interface for large droplets

of $\beta > 1$ are studied [Figs. 1(b) and 1(c)]. First, we present a theoretical background describing the relevant forces in the system.

A deformable object translating parallel to a rigid wall [Fig. 1(b)] experiences a wall repulsion force even at vanishing Reynolds numbers, known as noninertial lift force, which is given by [52]

$$F^+ \sim f(1-v)(\mu_M \dot{\gamma} R^3/h), \quad (1)$$

where v is the reduced volume, μ_M is the medium viscosity, $\dot{\gamma}$ is strain rate, R is the object radius, and h is the distance between wall and object center. The reduced volume is expressed as $v = 4V/[3\pi(S/4\pi)^{3/2}]$, where V is the enclosed volume and S is the surface area of the object; $f(1-v)$ is a function that denotes the deformability of the object, which monotonically increases with $(1-v)$. A deformable object, due to its shape change, renders $v < 1$ for which $f(1-v) > 0$ and experiences a nonzero F^+ . Consequently, the object tends to migrate towards a region of zero strain rate, $\dot{\gamma} = 0$, often at the channel center where the force vanishes and attains an equilibrium shape. On the other hand, for a rigid object such as a microbead, the shape change is negligible, rendering $v = 1$ and $f(1-v) = 0$, and consequently it does not experience noninertial lift force [52,53].

In the case of an object translating parallel to a deformable membrane or fluid-fluid interface, the hydrodynamic interaction between the object and interface can give rise to the deformation of the membrane or interface [49–51] [Fig. 1(c)], and such deformation tends to drive the object away from the interface [Fig. 1(b)]. For a deformable object such as a droplet in the vicinity of an unbounded fluid-fluid interface [50], fluid is driven outward from the front surface of the drop while fluid pulls in at the rear surface, resulting in an asymmetric shape of the interface. The interfacial deformation, coupled with the deformation of the drop due to its finite viscosity, drives the drop away from the interface. However, the lateral drift velocity of the drop was found to be a stronger function of the co-flow viscosity ratio than the drop-to-medium viscosity ratio [50].

Considering that an elastic membrane deforms similar to a fluid-fluid interface, the negative lift force experienced by a rigid object near a membrane can be adopted to that acting at an interface. For a sphere moving with a velocity V parallel to the interface, the negative lift force can be expressed as [49]

$$F^- \sim 6\pi\mu_M V_{dt} \frac{R^2}{z}, \quad (2)$$

where the drift velocity

$$V_{dt} \sim \frac{3\mu_M R^2 V^2}{25B} F(\tau H), \quad (3)$$

where z is the distance between the initially undeformed membrane and the object surface, τ and H are, respectively, nondimensional membrane tension and initial separation distance, and B is the membrane bending rigidity. $F(\tau H) = \int_0^\infty \frac{2k^4 K_0^2(k)}{k^4 + \tau H k^2} k dk$, where k is the magnitude of two-dimensional wave vector \mathbf{k} (k, θ) and K_0 is the order-zero modified Bessel function of the second kind [49].

By combining the interfacial and geometric parameters as φ , from Eqs. (2) and (3), we get

$$F^- \sim \frac{18\pi}{25} \mu_M^2 V^2 \frac{R^4}{z} \varphi. \quad (4)$$

Further, droplets at a fluid-fluid interface will experience a gradient of surface energy and migrate to a phase that offers the minimum energy state [Fig. 1(d)-ii]. The sign of the spreading parameter (S) decides the migration and is expressed as

$$S = \sigma_{1-3} - (\sigma_{1-2} + \sigma_{2-3}), \quad (5)$$

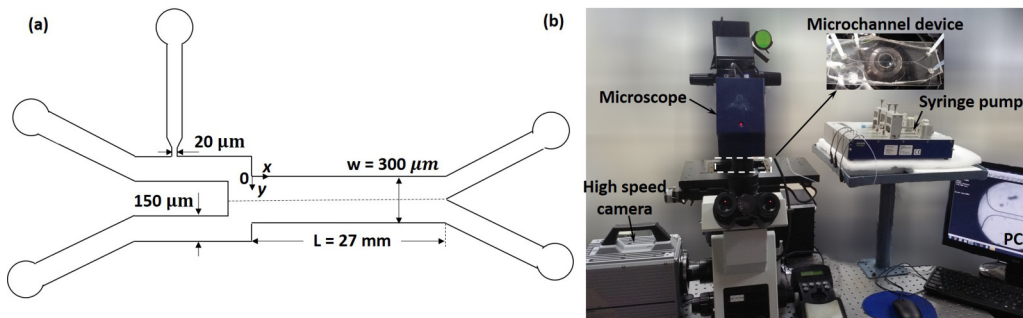


FIG. 2. A schematic (left) of the microchannel design and image of the experimental setup (right) including the microchannel device used in the present study.

where σ_{1-2} , σ_{2-3} , and σ_{1-3} is the IFT between P1 and P2, P2 and P3, and P1 and P3, respectively. We note that if $S > 0$, the drop in contact with the interface will migrate [42] from P1 to P2, or else it will continue to flow along with P1.

III. EXPERIMENTAL

A schematic and experimental image of the microfluidic setup used in the present study are depicted in Fig. 2. The device comprises two inlet channels leading to an expanded channel region—one of the inlet channels features a T junction for producing droplets. The expanded channel is $300 \mu\text{m}$ wide (W), $100 \mu\text{m}$ deep, and 27 mm long (L) of rectangular cross section. The device was fabricated in poly dimethyl siloxane (PDMS) using standard soft lithography [54]. We exposed the channels and glass slide to oxygen plasma for 3 min at 30 W RF power. Immediately after plasma exposure, the microchannel device was bonded onto the glass slide. Due to the oleophilic nature of native PDMS, the generation of oil droplets in the device requires hydrophilic surface treatment of the channels [55,56]. After mild heating at $50 \text{ }^\circ\text{C}$ for 5 min, the channel was flushed with polyethylene glycol (PEG) for 30 min to render hydrophilic surfaces, enabling the generation of oil droplets. PEG (molecular wt. 35 000), castor oil, silicone oil 20/100/1000, olive oil, and FC-40 oil were procured from Sigma-Aldrich, USA. PEG at 15% w/w was added to deionized water to obtain the Newtonian aqueous solution. Density and viscosities of the fluids were measured using a viscometer (Stabinger ViscometerTM, Anton Paar, Austria) and Anton Paar Rheometer MCR 72 with 50 mm of cone diameter at $25 \text{ }^\circ\text{C}$ and verified with the existing literature. IFT was measured using a Droplet Size Analyzer (DSA 25, Krüss GmbH, Germany). The measured properties of the fluids are summarized in Table I. Each measurement was repeated at least thrice and the standard deviation was found to be within $\pm 3\%$. PEG is used as the first co-flow stream (P1) and one of the following oils, silicon oil 100 (SiO-100), SiO-20, FluorinertTM (FC)-40, or olive oil, is used as the second co-flow stream (P2), and castor oil, SiO-1000, SiO-100, and FC-40 are used as droplet phase (P3). The working fluids are infused into the channels using high-performance syringe pumps (Cetoni GmbH, Germany). The fluidic connection between syringe pumps and the device is established using polytetrafluoroethylene tubing (Fisher Scientific, USA). Droplet motion was observed and captured using an inverted microscope (Olympus IX73) coupled with a high-speed monochrome camera (FASTCAM SA3 model, Photron USA, Inc.) operating at 125 to 1000 fps, interfaced with a PC via PHOTRON FASTCAM VIEWER software.

IV. RESULTS AND DISCUSSION

Here, PEG and an immiscible oil are infused into a microchannel as P1 and P2 [Fig. 1(a)], respectively, to establish an immiscible co-flow system with a stable interface. The flow rates of

TABLE I. The measured properties of the different fluids used in the present study.

Individual fluid	Density, ρ (kg/m ³)	Viscosity, μ (mPa s)	Viscosity contrast, $\Delta\mu$ (mPa s)	IFT, σ (mN/m)
PEG 15% wt/wt	1029	58		
Castor oil	960	650		
SiO-1000	1100	1000		
SiO-100	960	100		
SiO-20	970	20		
Olive oil	917	80		
FC-40	1850	4		
Co-flow combination				
PEG-Castor oil			592	16-20
PEG- SiO-1000			942	17
PEG-SiO-100			42	20
PEG-SiO-20			38	12.39–14.2
PEG-Olive oil			22	12.78–12.80
PEG-FC-40			54	30
PEG-SiO-100+Span 80			942	1–2
Castor oil-FC-40			646	12.62
Castor oil-SiO-100			550	5-7
Castor oil-SiO-20			630	0.13
SiO-20-FC-40			16	6.3
Olive oil-FC-40			76	11.38
Olive oil-SiO-1000			920	1
P1-P2-P3	σ_{1-2}	σ_{2-3}	σ_{3-1}	Spreading parameter (S)
PEG-FC40-Castor oil	16	30	12.62	<0
PEG-SiO-100-Castor oil	16	21.4	6	<0

PEG and the co-flowing immiscible oil phase are varied in the range of 0.5 to 3 $\mu\text{l}/\text{min}$ and 2 to 30 $\mu\text{l}/\text{min}$, respectively. The droplet phase (P3) is an oil that is immiscible with both PEG and the co-flowing oil (P2) and is infused at a flow rate in the range of 0.1 to 1.0 $\mu\text{l}/\text{min}$. At the above flow-rate conditions, $\text{Re}_i = (\rho_i u_i d_{hi}/\mu_i) \ll 1$, so we safely ignore inertial forces. Here, ρ_i , μ_i , u_i , and d_{hi} are, respectively, the density, viscosity, velocity, and hydraulic diameter of the phases, and $i = 1, 2, 3$. We found that the entrance effects are only significant for $x \leq 500 \mu\text{m}$, but since our region of interest lies at $x \geq 3000 \mu\text{m}$, we take fully developed flow conditions for our analysis. The capillary numbers, $\text{Ca}_i = \mu_i u_i/\sigma_{ij}$ (σ_{ij} = interfacial tension between phases i and j) of the different phases are estimated to be $\text{Ca}_1 = \mu_1 u_1/\sigma_{12} = 0.001-0.014$, $\text{Ca}_2 = \mu_2 u_2/\sigma_{12} = 0.004-0.05$, and $\text{Ca}_3 = \mu_3 u_3/\sigma_{13} = 0.003-0.1$. We present and discuss our investigation in two parts: first, we explore the lateral migration of small droplets of $D < W_1$, where D is droplet diameter and W_1 is the width of the suspending phase (P1). Subsequently, we study interfacial instability with large droplets of $D \geq W_1$.

A. Lateral migration of small droplets ($\beta < 1$) in a stable co-flow system

A stable interface is critical to the controlled manipulation of objects in a co-flow system [41,42]. Here, our objectives are to study lateral migration and interface deformation due to the interaction between droplets and the co-flow interface. Therefore, initially in the absence of droplets, a stable co-flow system is ensured to avoid the effect of the inherent instability of the system. Experimental image of an initially stable interface in the absence of droplets with PEG as P1 and SiO-100 as P2 is presented in Fig. 3(a)-i. The interface is curved at the entry region of the expanded channel satisfying

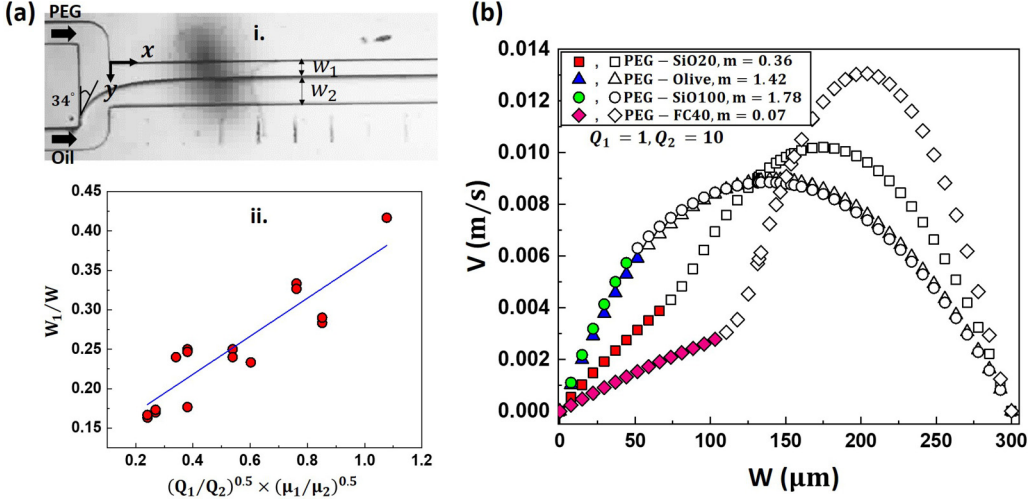


FIG. 3. (a)-i Experimental image of a stable interface in the absence of droplets with PEG as P1 and SiO-100 as P2. (a)-ii Variation of the interface location with the ratio of flow rates and viscosities of the co-flowing phases. (b) Velocity profiles for the different combinations of fluids used to establish co-flow, $m = (\mu_2/\mu_1)$.

the contact angle criterion at the interface of PDMS, PEG, and SiO-100 at the channel wall but far away from this region, the interface is flat, where we study the dynamics. Due to hydrophilic surface treatment, the PEG-PDMS contact angle in the entry region is 34° , complying with literature [57] and explaining the curved nature of the interface. We find that the interface location is strictly controlled by the ratio of flow rates and viscosities of the co-flowing streams, as shown in Fig. 3(a)-ii, in agreement with the literature [39]. Literature reports that in a co-flow system, instability could be triggered due to a viscosity and density difference, and inflection in velocity profile across the interface or inertia [9]. Velocity profiles were obtained for the different combinations of fluids used to establish co-flow which show a more prominent inflection point for a lower viscosity ratio (m), as shown in Fig. 3(b) and Fig. S1 in Supplemental Material [58]. The KH instability that arises when two adjacent fluid layers are in relative motion will be suppressed if the following condition is satisfied [2]:

$$(V_1 - V_2)^2 < 2 \left(\frac{\rho_1 + \rho_2}{\rho_1 \rho_2} \right) \sqrt{\sigma g (\rho_1 - \rho_2)}, \quad (6)$$

where V_1 and V_2 are the velocities and ρ_1 and ρ_2 are densities of P1 and P2, respectively. In the present study, considering the densities of P1 and P2 (see Table I) and corresponding flowrates 2–5 $\mu\text{l}/\text{min}$ and 5–10 $\mu\text{l}/\text{min}$, respectively, we estimate that the left – hand side $\sim 10^{-6}$ and right – hand side $\sim 10^{-2}$, implying KH instability can be neglected in the present case. We rule out the presence of Rayleigh-Plateau instability as no spatial or temporal growth of disturbance was observed at the interface and achieved a stable co-flow regime for $Ca_1 \approx Ca_2$ and $Ca_{1,2} > 0.001$. Literature suggests that bulk mode interfacial instability can appear at high Re due to the onset of turbulence [17,35]; we eliminate such possibility as in our case $Re \ll 1$.

Given a stable interface between the co-flowing streams, we now turn to understand the lateral migration of smaller droplets of confinement ratio, $\beta = (D/W_1) < 1$. The lateral migration of castor oil droplets of $\beta = 0.5$ and 0.75 in a co-flow of PEG and SiO-100 is presented in Fig. 3. From literature [32,45], we note that deformable objects at low –Re condition will migrate towards the maximum velocity or zero strain-rate region closer to the interface under the influence of noninertial lift (NIL) force (F^+). Further, from our previous work, we recall that castor oil droplets in PEG should migrate laterally to the channel center due to the sole effect of the NIL force [59]. In the

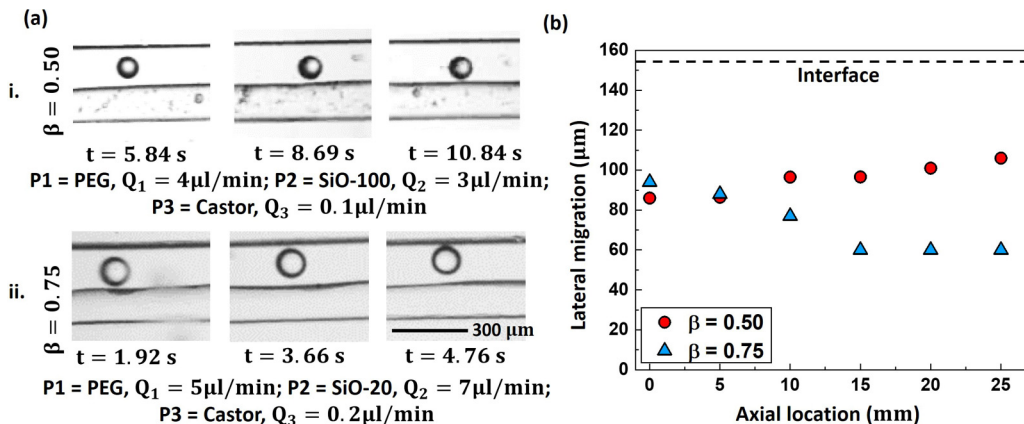


FIG. 4. (a) Experimental image showing the lateral migration behavior of small droplets ($\beta < 1$): (a-i) Smaller droplets ($\beta < 0.5$) migrate toward the interface; (a-ii) Larger droplets ($\beta > 0.5$) drift away from the interface. (b) Plot showing the lateral position of smaller and larger droplets as they flow downstream (x direction).

present case, as the zero strain-rate region is in the SiO-100 phase [see Fig. 3(b)], it is expected that the noninertial lift will drive all the droplets initially present in the PEG phase towards the interface. However, we observe although smaller droplets of $\beta \leq 0.5$ migrate towards the interface, surprisingly, larger droplets of $\beta > 0.5$ are observed to drift away from the interface, as depicted in Figs. 4(a-i) and 4(a-ii). This unexpected observation indicates the presence of a negative lift (NL) force (F^-) [see Eq. (2)] that acts in a direction away from the interface and opposite to the noninertial lift force, which arises due to the lubrication pressure in the fluid film between a drop and interface [49].

To explain the contrasting migration behavior of the smaller and larger droplets, we take the ratio of the NIL and NL forces given in Eqs. (1) and (2) as follows:

$$k = \frac{F^+}{F^-} \approx \frac{f(1-v)z\dot{\gamma}}{R\mu hV^2\phi}. \quad (7)$$

We see that the force ratio, $k \propto R^{-1}$, suggesting that the smaller droplets will experience a dominant NIL force and hence migrate toward the interface. On the other hand, larger droplets will experience a stronger NL and therefore migrate away from the interface. The explanation of the contrasting migration behavior of droplets in terms of their confinement ratio, β is given in Sec. S5 in Supplemental Material [58]. Our observation with droplets is in contrast with the migration dynamics observed in the case of rigid microparticles wherein even the smaller particles also migrate away from the elastic membrane, albeit at a lower migration velocity compared to bigger ones [49]. Evidently, the inherent deformability-induced noninertial lift force contributes to this apparent discrepancy. The existence of a negative-lift force also highlights that for interfacial migration of deformable objects, the channel width should be adjusted according to the object size to ensure $\beta < 0.5$, and explains interfacial migration of cells that satisfy the above criterion along [45] in addition to a favorable spreading parameter [42]. Further, considering, $\text{Re} \ll 1$, we find viscocapillary length scale, $(\mu^2/\rho\sigma) \approx 140 \mu\text{m}$, is greater than droplet size and interdistance, thus satisfying the criterion for “soft swimming,” or drifting away from the fluid-fluid interface, at vanishing Reynolds numbers [51].

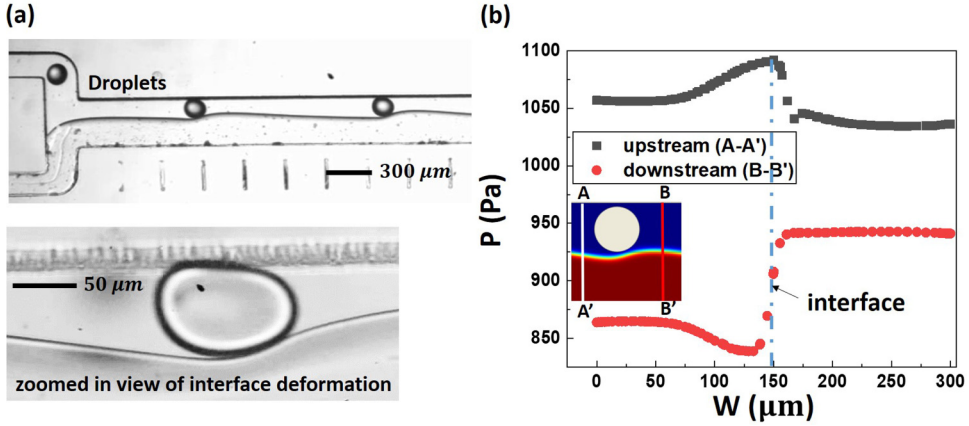


FIG. 5. (a) Experimental image and simulation results showing interfacial instability caused by a castor oil droplet having a confinement ratio, $\beta = 1.1$, to an initially stable and flat interface between co-flowing streams of PEG at flow rate $2 \mu\text{l}/\text{min}$ and SiO-100 oil at a flow rate $5 \mu\text{l}/\text{min}$. (b) Numerical simulation results showing the variation of pressure across the channel width at upstream and downstream of a droplet.

B. Interfacial instability with large droplets ($\beta \geq 1$)

As discussed, the presence of NL force (F^-) tends to push droplets of $\beta < 1$ away from the interface, and therefore it is difficult to achieve an interaction between these small droplets and the interface. To facilitate droplet-interface contact and interaction, larger droplets having a confinement ratio, $\beta > 1$, are used. Literature shows that droplets contacting a co-flow interface can migrate either owing to the NIL force [39] and a favorable spreading parameter [42], $S > 0$. In the present case, using the IFT values presented in Table I, we find that $S < 0$. Due to a strong NL force and unfavorable spreading parameter, interfacial migration does not occur, offering a system that is suitable for studying interfacial deformation.

The interfacial instability caused by a castor oil droplet of confinement ratio, $\beta = 1.1$, to an initially stable and flat interface between co-flowing streams of PEG at a flow rate of $2 \mu\text{l}/\text{min}$ and SiO-100 oil at a flow rate of $5 \mu\text{l}/\text{min}$ is presented in Fig. 5(a). As observed, in the absence of interfacial migration, droplets are squeezed between the interface and the wall giving rise to a marked deformation of both the drop and the interface. The profile of the resulting wavy interface can be characterized by the wave amplitude (A), and wavelength (λ) of deformation [Fig. 1(c)], and the wave speed (u_w), where A is taken as the difference between the SiO-100 oil sidewall to wave peak distance (w') and undeformed width of the SiO-100 oil phase (w_2), i.e., $A = (w' - w_2)$, and λ is measured as the distance between two consecutive wave peaks [Fig. 1(c)]. As the interface waviness is solely attributed to the presence of droplets, the wave peaks are formed adjacent to the droplets and move with the droplets. So, λ is always equal to the droplets spacing (s), and u_w is always the same as the droplet speed (u_d) as the wave peaks remain in contact with droplets while propagating downstream. The viscous length scale [11], $l \sim \sqrt{\mu/\rho\dot{\gamma}}$, is estimated by considering a co-flow of PEG–SiO-100 at flowrates 2 and $5 \mu\text{l}/\text{min}$, respectively, and found to be $l \sim 2.5 \mu\text{m}$. Here, we find that $\lambda \gg l$, implying we can only observe long waves [9,11] in the present case.

To find the possible source of interfacial deformation and explain the waviness pattern, we performed simulations with a droplet approximated as a particle of $120\text{-}\mu\text{m}$ diameter placed in the PEG phase in a PEG–SiO-100 co-flow. The details of the numerical model are presented in Sec. S2 in Supplemental Material [58]. The interface shape obtained from the simulations compares well with that observed in experiments, as shown in Fig. 5(a). We obtain the pressure profiles along the two cutlines across the width at upstream, line A–A', and downstream, line B–B', as shown in Fig. 5(b). The pressure profile along line A–A' reveals that the pressure in the PEG phase is higher

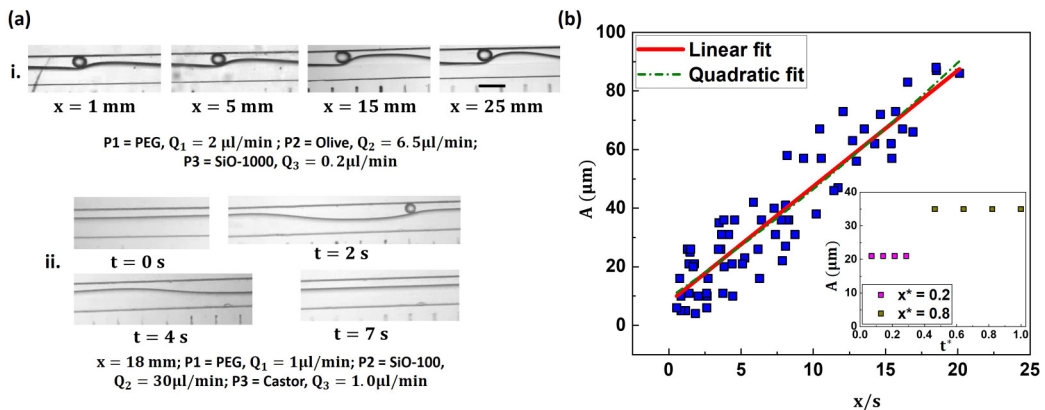


FIG. 6. (a) Experimental image showing the (i) growth of wave amplitude (A) along the flow direction (x), and (ii) quick dampening of interfacial instability at a fixed location ($x = 18 \text{ mm}$). (b) Variation of wave amplitude (A) with location along the flow direction (x); inset shows the variation of wave amplitude (A) at a fixed location with time (t).

than that in the oil phase upstream of the droplet, and as a result, the curvature is positive on the PEG side, similar to that observed in experiments. On the contrary, pressure is higher in the SiO-100 phase than that in the PEG phase downstream of the droplet, resulting in a positive curvature in the SiO-100 phase. The presence of a larger droplet having $\beta > 1$ in the PEG phase constricts the flow of the surrounding phase (P1) which gives rise to pressure buildup upstream of the droplet, and there is a significant pressure jump across the droplet. However, pressure drop across the same axial length as the droplet diameter in the SiO-100 phase is relatively small, which explains a higher pressure in the SiO-100 phase downstream of the droplet.

C. Evolution of wave amplitude along the flow direction

For a planar co-flow with viscosity stratification, the literature assumes a complex exponential growth of amplitude with space and time as a solution to the Orr-Sommerfeld perturbation equation solved for both the phases [34]. In stark contrast, here we find that wave amplitude (A) grows linearly along the flow direction (x), as evident from the results in Figs. 6(a)-i and 6(b), which is obtained for a different combination of operating flow rates and properties of the co-flowing streams: $Q_1 = 1-3 \mu\text{l/min}$, $Q_2 = 2-8 \mu\text{l/min}$, $\sigma = 12-20 \text{ mN/m}$, $\Delta\mu = 22-42 \text{ mPa} \cdot \text{s}$, $\beta = 1.1 \pm 0.2$. Here, the location along the flow direction is normalized by the spacing between adjacent droplets (s). It is found that at a fixed axial location, the wave amplitude (A) is higher for a smaller spacing (s) between adjacent droplets, as shown in Fig. S3 [58]. We also find that at a fixed axial location, the interfacial deformation is quickly suppressed once a droplet passes through that particular location [see Fig. 6(a)-ii].

We now attempt to theoretically explain the variation of the wave amplitude (A) with distance along the flow direction. Taking a cue from the literature [34], we can write the normal stress balance equation across a curved interface [see Fig. 1(d)-i] as follows:

$$\left(p' - 2\mu \frac{\partial v'}{\partial y} \right)_{P2} - \left(p' - 2\mu \frac{\partial v'}{\partial y} \right)_{P1} = \sigma \frac{d^2 A}{dx^2}, \quad (8)$$

where p' is the perturbation pressure and v' is the perturbation velocity in the y direction, and μ is the dynamic viscosity. The normal stress balance equation [Eq. (8)] used in our case has been used in the literature for viscosity-stratified flows bounded by two parallel plates [34]. A similar approach has also been taken for stratified flow in a rectangular duct [20]. Here, the origin is at the interface,

and y is taken to be positive into the P1 side. By rearranging Eq. (8), we get

$$\frac{d^2 A}{dx^2} = \frac{1}{\sigma} \left(\Delta p' - 2\Delta\mu \frac{\partial v'}{\partial y} \right). \quad (9)$$

Upon integrating both sides with respect to x , we get

$$A = \frac{1}{\sigma} \left(\Delta p' - 2\Delta\mu \frac{\partial v'}{\partial y} \right) x^2 + c_1 x + c_2. \quad (10)$$

Imposing the following boundary conditions: (i) at $x = 0$, $A = A_{\min}$ and (ii) at $x = \delta$, $A = A_{\max}$, we get $c_2 = A_{\min}$, $c_1 = \left(\frac{A_{\max} - A_{\min}}{\delta} - \left(\frac{\Delta p'_\delta - 2\Delta\mu \frac{\partial v'}{\partial y}}{\sigma} \right) \delta \right)$, where $\Delta p'_\delta$ is the perturbation pressure drop across the interface at $x = \delta$.

Upon substituting c_1 and c_2 in Eq. (10), we get

$$A = \frac{1}{\sigma} \left(\Delta p' - 2\Delta\mu \frac{\partial v'}{\partial y} \right) x^2 + \left(\frac{A_{\max} - A_{\min}}{\delta} - \frac{\Delta p'_\delta - 2\Delta\mu \frac{\partial v'}{\partial y}}{\sigma} \delta \right) x + A_{\min}. \quad (11)$$

Here, we scale $\frac{\partial v'}{\partial y} = \frac{A_{\max} - A_{\min}}{w_1 \Delta t}$, where Δt is the time required for a droplet to travel the entire channel length, where w_1 is the width of the P1 phase. Following the analysis outlined in Sec. S4 [58], Eq. (11) takes the following form where we find that the coefficient of x^2 is greater than the coefficient of x ; hence, the former will have a dominating effect on A :

$$A = \frac{1}{\sigma} \left(\Delta p' - 2\Delta\mu \frac{\partial v'}{\partial y} \right) x^2 + \left(-\frac{\Delta p'_\delta}{\sigma} \delta \right) x + A_{\min}. \quad (11a)$$

From the coefficient of the leading-order terms, we note that the wave amplitude (A) increases as (i) IFT (σ) between the co-flowing phases decreases, (ii) viscosity difference across the interface $\Delta\mu$ decreases, and (iii) pressure difference across the interface $\Delta p'$ increases, which happens for a larger droplet diameter [60]. The above theoretical expression for A that assumes stratified flow configuration bounded by parallel plates [34] reveals a quadratic growth in the wave amplitude contrary to a linear growth observed in our experiments. The difference can be attributed to a strong confinement effect in the actual experiments which tends to suppress the growth rate of the wave amplitude leading to a linear variation of wave amplitude [22,33]. The functional relationship of A with $\Delta\mu$, σ , and $\Delta p'$ obtained from Eq. (11) or (11a) is further validated with experimental data in the next section.

The growth of wave amplitude (A) along the flow direction (x) is accompanied by an increase in the interfacial curvature around the droplet, as evident from the experimental images in Fig. 6(a), and we attempt to predict the same analytically. For a droplet placed at an arbitrary location x , as shown in Figs. 1(c) and 1(d)-i, we can write

$$p_{in} - n(\Delta p - G) = p^{\mu 1} = p^{d 1} + \Delta p = p^{d 2} - \frac{\sigma}{r_d} + \Delta p = p_{in} \left(1 - \frac{x}{L} \right) - \frac{\sigma}{r_d} + \Delta p, \quad (12)$$

where p_{in} is the inlet pressure of the channel of length L , Δp and G are, respectively, the pressure drop across a droplet of diameter D and pressure gain in the spacing (s) between two consecutive droplets, n is the number of droplets, $n = x/(D + s)$ in the upstream, $p^{\mu 1}$, $p^{d 1}$, and $p^{\mu 2}$, $p^{d 2}$ are upstream and downstream pressures across the droplet in P1 and P2 phases, respectively, and r_d is the interface curvature downstream of a droplet [Fig. 1(d)-i]. By rearranging Eq. (12), we get

$$\frac{\sigma}{r_d} = -p_{in} \left(\frac{x}{L} \right) + \Delta p + n(\Delta p - G). \quad (13)$$

Substituting for the number of droplets n and $\Delta p = p^{u1} - p^{d1} = (p^{u2} + \frac{\sigma}{r_u}) - (p^{d2} - \frac{\sigma}{r_d}) = (p^{u2} - p^{d2}) + (\frac{\sigma}{r_u} + \frac{\sigma}{r_d}) = p_{in} \frac{D}{L} + (\frac{\sigma}{r_u} + \frac{\sigma}{r_d})$ in Eq. (13), we get

$$\frac{\sigma}{r_d} = p_{in} \left(\frac{D+s}{L} \right) + G - \left(p_{in} \frac{D}{L} + \frac{\sigma}{r_u} \right) \left(1 + \frac{D+s}{x} \right), \quad (14)$$

where r_u is the interface curvature at the upstream of a droplet. Considering G to be the same between any pair of adjacent droplets, by taking the derivative of both sides of Eq. (14), we get

$$\frac{dr_d}{dx} = -\frac{r_d^2}{\sigma} \left[p_{in} \frac{D}{L} \left(\frac{D+s}{x^2} \right) + \frac{\sigma}{r_u^2} \left(\frac{dr_u}{dx} \right) + \frac{\sigma}{r_u} \left(\frac{D+s}{x^2} \right) + \frac{\sigma}{r_u} \left(\frac{dr_u}{dx} \right) \left(\frac{D+s}{x} \right) \right]. \quad (15)$$

Experimental images in Fig. 6(a) show that the upstream curvature is significantly smaller than that at the downstream, i.e., $r_u \gg r_d$, and $\frac{dr_u}{dx}$ is small; hence, the second and third terms within the bracket on the right-hand side can be ignored. Evidently, the remaining terms inside and outside the bracket are positive, $\frac{dr_d}{dx} < 0$, suggesting that r_d should decrease and the interfacial curvature will increase along the flow direction. This is in agreement with experimental results that show that the interfacial curvature and consequently the amplitude of the wave that is carried along with the droplet grows spatially in the flow direction. Further, the wave amplitude for all the drops that pass through a fixed location at different times is found to be the same and thus is independent of time, as shown in the inset of Fig. 6(b). This confirms the convective nature of instability and rules out the presence of absolute instability, explaining why the disturbance is quickly suppressed once a droplet passes through a particular location.

D. Effect of co-flow IFT, viscosity contrast, and confinement on the spatial growth of wave amplitude

It has been shown that viscosity, IFT, inertia, and the presence of walls can have a significant effect on the stability of multiphase systems [9,33,34]. Here, we study the effect of viscosity contrast ($\Delta\mu$), IFT (σ), and confinement ratio (β) on the wave amplitude (A) using the co-flows of different combinations of fluids presented in Table I and castor oil droplets, as shown in Figs. 7(a) and 7(b). In all cases, we find that the wave amplitude increases linearly along the flow direction, in agreement with the results presented in Fig. 6(a). As observed, the wave amplitude is found to be a minimum for a co-flow of PEG-FC40 combination having $\Delta\mu = 54$, $\sigma = 30$ mN/m and maximum for PEG-SiO-20 having $\Delta\mu = 38$, $\sigma = 13$ mN/m. Intermediate values of wave amplitudes are observed for PEG-SiO-100 having $\Delta\mu = 42$, $\sigma = 20$ mN/m and PEG-olive oil having $\Delta\mu = 22$, $\sigma = 12.8$ mN/m.

We see that except for the PEG-SiO-20 combination, a higher wave amplitude is observed in for a co-flow with a smaller IFT (σ) and smaller viscosity contrast ($\Delta\mu$), in agreement with the predictions of Eq. (11). For the wall-bounded case, it is argued that if one of the phases is highly viscous, the interface takes a long time to deform [34]; similarly, it has been shown that IFT has a stabilizing effect on the instability [2,4]. The slopes of the curves indicating the spatial growth in the amplitude along the flow direction are found to be higher at a smaller IFT, in agreement with Eq. (11). PEG-SiO-20 co-flow has a higher viscosity contrast but a smaller IFT. So, the nonmonotonic variation in the wave amplitude with the variation in viscosity contrast ($\Delta\mu$) and IFT (σ) could perhaps be attributed to the fact that both the parameters can affect the wave amplitude, as evident from Eq. (11).

In the combinations of fluids used in our co-flow systems, the viscosity contrast and IFT vary simultaneously, so in order to understand the sole effect of viscosity contrast at a fixed IFT and vice versa, we turn to numerical simulations. For a fixed $\Delta\mu = 24$, we varied IFT in the range 1 to 30 mN/m and for a fixed IFT ($\sigma = 20$ mN/m), viscosity contrast is varied in the range 24 to 52. We find that wave amplitude (A_σ) decreases linearly with an increase in IFT (σ), as shown in Fig. 7(c), revealing the stabilizing effect of a higher IFT, in agreement with literature [16,35]. We find that wave amplitude ($A_{\Delta\mu}$) decreases monotonically with an increase in the viscosity contrast ($\Delta\mu$), as

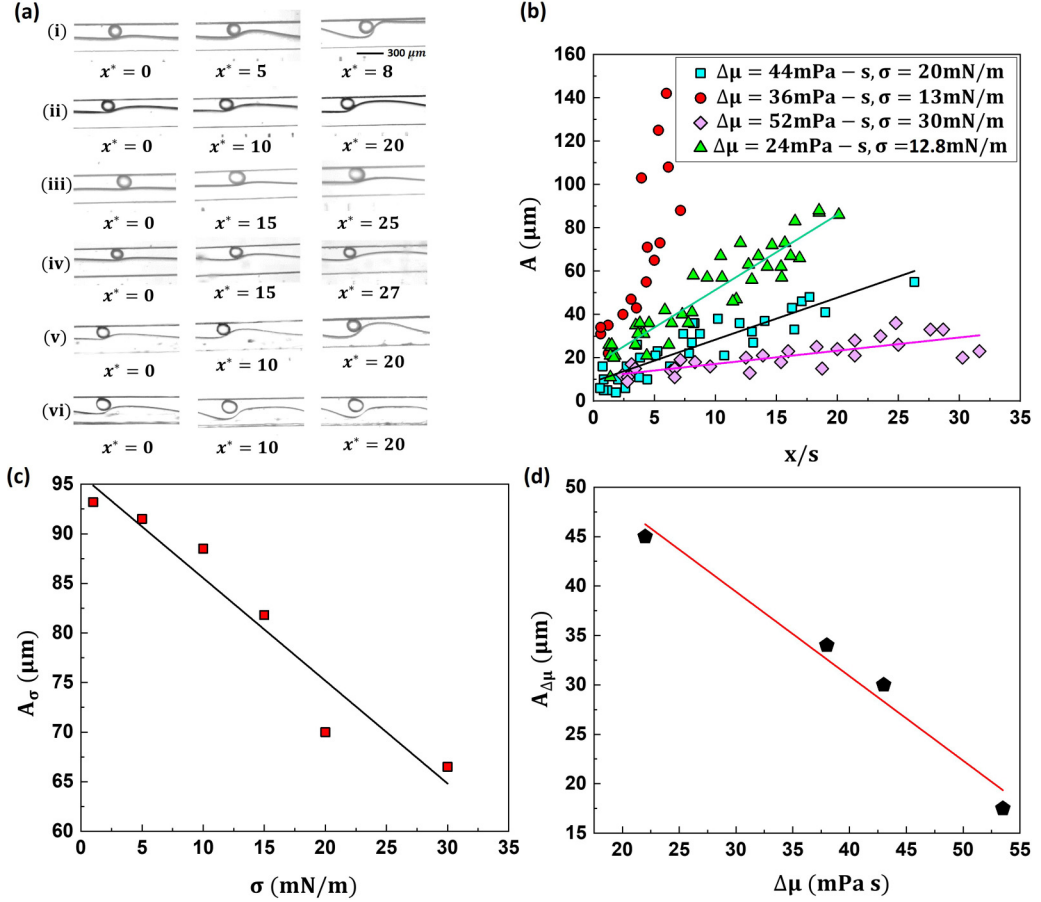


FIG. 7. (a) Experimental images showing interface deformation, from top to bottom: (i) $P1 = \text{PEG}$, $P2 = \text{SiO-20}$, $P3 = \text{Castor}$; (ii) $P1 = \text{PEG}$, $P2 = \text{Olive}$, $P3 = \text{SiO-1000}$; (iii) $P1 = \text{PEG}$, $P2 = \text{FC-40}$, $P3 = \text{Castor}$; (iv) $P1 = \text{PEG}$, $P2 = \text{SiO-100}$, $P3 = \text{Castor}$; (v) $P1 = \text{PEG}$, $P2 = \text{SiO-100+5\% SPAN}$, $P3 = \text{Castor}$; (vi) $P1 = \text{PEG}$, $P2 = \text{SiO-100+15\% SPAN}$, $P3 = \text{Castor}$. In all cases, $Q_1 = 2-5 \mu\text{l/min}$, $Q_2 = 5-30 \mu\text{l/min}$. (b) Variation of wave amplitude (A) along flow direction (x) using co-flows of a different combination of fluids having different viscosity contrast ($\Delta\mu$) and IFT (σ). (c) Variation of wave amplitude (A_σ) with an increase in IFT (σ), for a fixed viscosity contrast $\Delta\mu$. (d) Variation of wave amplitude ($A_{\Delta\mu}$) with an increase in viscosity contrast $\Delta\mu$, for a fixed IFT (σ).

shown in Fig. 7(d). We see from Eq. (11a) that the magnitude of the first term on the right-hand side decreases with an increase in $\Delta\mu$, which explains the monotonic variation observed.

Further, unlike the effect of IFT, literature depicts a rather complex effect of viscosity contrast on the stability of multiphase systems [9]. While viscosity promotes dissipation of energy, an opposite effect in terms of the production of kinetic energy disturbance could offset the dampening effect [9]. In the case of co-flow of PEG-FC40 combination having $\Delta\mu = 54$ and $\sigma = 30$ mN/m. Here, both these values are highest among all combinations used and therefore have a deterring effect on the wave amplitude. For PEG-SiO 20 having $\Delta\mu = 38$ and $\sigma = 13$ mN/m, PEG-olive oil having $\Delta\mu = 22$ and $\sigma = 12.8$ mN/m, as both the IFT and viscosity contrast values are the lowest among all among all combinations, it has an amplifying effect on the wave amplitude. For PEG-SiO 100 having $\Delta\mu = 42$ and $\sigma = 20$ mN/m the values are moderate, giving rise to an intermediate wave amplitude observed.

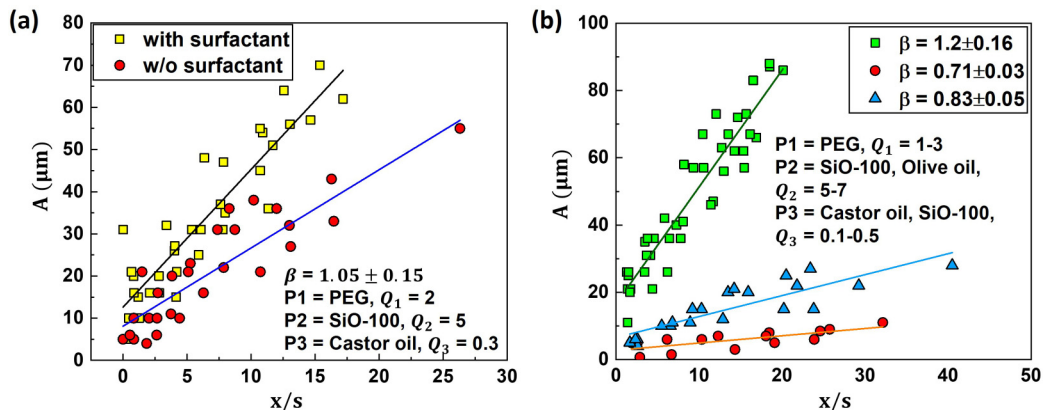


FIG. 8. (a) Variation of wave amplitude in the flow direction (x) with and without the addition of surfactant inducing a change in IFT at a fixed viscosity contrast ($\Delta\mu$ ($\beta = 1.05 \pm 0.15$; P1 = PEG, $Q_1 = 2 \mu\text{l}/\text{min}$; P2 = SiO-100, $Q_2 = 5 \mu\text{l}/\text{min}$; P3 = Castor oil, $Q_3 = 0.3 \mu\text{l}/\text{min}$)).(b) Variation of wave amplitude in the flow direction (x) for different droplet confinement ratios (β) (P1 = PEG, $Q_1 = 1-3 \mu\text{l}/\text{min}$; P2 = SiO-100, Olive oil, $Q_2 = 5-7 \mu\text{l}/\text{min}$; P3 = Castor oil, SiO-100, $Q_3 = 0.1-0.5 \mu\text{l}/\text{min}$).

Further, we experimentally study the effect of variation of IFT through the addition of surfactants without altering the viscosity of the phases and hence at a fixed viscosity contrast. Surfactant Span 80 is added at 5–15% wt/wt to the SiO-100, and experiments were performed with a co-flow system of PEG–SiO-100 and castor oil droplets of $\beta = 1.05 \pm 0.15$ in PEG. The IFT of the interface and viscosity values at different %wt/wt of Span 80 is presented in Table I. We observe that the addition of surfactant greatly reduces co-flow IFT and therefore results in a higher amplitude, as shown in Fig. 7(c). A higher slope of the line in case of a lower IFT is also evident from Fig. 8(a) and Eq. (11). The effect of droplet confinement ratio (β) on the interfacial instability is also studied. We find that for all combinations of fluids, a higher β leads to a higher wave amplitude, which is shown in Fig. 8(b). The pressure jump across the droplet Δp can be related to wall shear stress (τ) as $\Delta p S_f = \tau S_s = \mu \dot{\gamma} S_s$, where S_f is the projected frontal area of the droplet along the flow direction and S_s is the surface area of the droplet. An object placed in a flow field will give rise to an increase in the strain rates ($\dot{\gamma}$) at the channel walls and the surface of the object [61]. Moreover, a larger droplet would force the fluid to assume a higher velocity through the gap between the droplet and the walls to satisfy continuity, resulting in higher shear stress compared to a smaller droplet. Taking S_s/S_f is independent of droplet size, Δp will be higher for a bigger droplet, resulting in a higher wave amplitude as observed. Further, we see that a larger droplet gives rise to a faster increase in the wave amplitude in the flow direction, as indicated by a significantly higher slope of the curve, which is also depicted by Eq. (15) and Eq. (11) in terms of Δp . We also find that at a fixed axial location, the curvature and hence the wave amplitude (A) are higher for a smaller spacing (s) between adjacent droplets, as shown in Fig. S3 [58], in agreement with Eq. (15).

V. CONCLUSIONS

We experimentally studied the interaction between droplets and the interface of a pair of co-flowing immiscible streams, leading to lateral migration of droplets and interfacial deformation. Lateral migration was observed for small droplets of confinement ratio, $\beta < 1$. We found smaller droplets of $\beta < 0.5$ migrate towards the interface whereas to our surprise larger droplets of $0.5 < \beta < 1$ migrate away from the interface. We showed the interplay between wall-directed negative lift force and the centerward noninertial lift force underpin the phenomena. We showed the ratio of NIL force to NL force is inversely proportional to droplet size, explaining the size-based contrasting migration behavior. Deformation waves were observed in an initially stable and flat interface in the

presence of larger droplets of $\beta > 1$, which propagate downstream similar to the traveling peristaltic waves. From numerical simulations, we showed that interfacial deformation is a consequence of the differential pressure jumps across the co-flow interface at the upstream and downstream regions of a droplet. In the upstream region, pressure in the droplet-carrying phase is higher whereas that in the downstream region is smaller, which explained the interfacial curvatures observed. We found that the amplitude of the deformation wave caused by a particular droplet grows spatially downstream but is the same for a train of droplets crossing a particular location, suggesting the contribution of convective instability. We studied the influence of co-flow interfacial tension, viscosity contrast, confinement ratio, and droplet spacing on the deformation wave amplitude and its variation along the flow direction. While a higher IFT has a stabilizing effect leading to a reduction in wave amplitude, viscosity contrast has a nonmonotonic effect and further wave amplitude was found to be higher for a higher confinement ratio and smaller droplet spacing. Our study elucidates the behavior of droplet migration and droplet-induced interfacial deformation in a co-flow system which may find relevance in droplet-based microfluidic systems.

ACKNOWLEDGMENTS

This work was supported by IIT Madras via Project No. RF21220988MERFIR008509, and by the Ministry of Human Resources and Development, Government of India, through the Institute of Eminence (IoE) scheme via Grant No. 11/9/2019-U.3(A).

-
- [1] P. A. M. Boomkamp and R. H. M. Miesen, Classification of instabilities in parallel two-phase flow, *Int. J. Multiphase Flow* **22**, 67 (1996).
 - [2] S. Chandrasekhar, Hydrodynamic and Hydromagnetic Stability (Chandrasekhar).pdf, 1961.
 - [3] Plateau, in *Experimental and Theoretical Statics of Liquids Subject to Molecular Forces Only* (Gauthier-Villars, Paris, 1873), Vol. 1, pp. 1–427.
 - [4] D. Barnea and Y. Taitel, Kelvin-Helmholtz stability criteria for stratified flow: Viscous versus non-viscous (inviscid) approaches, *Int. J. Multiphase Flow* **19**, 639 (1993).
 - [5] L. Rayleigh, Investigation of the character of the equilibrium of an incompressible heavy fluid of variable density, *Proc. R. Soc. London, Ser. A* **14**, 170 (1883).
 - [6] G. I. Taylor, The instability of liquid surfaces when accelerated in a direction perpendicular to their planes, II. *Proc. R. Soc. London, Ser. A* **202**, 81 (1950).
 - [7] P. G. Saffman and G. I. Taylor, The penetration of a fluid into a porous medium or Hele-Shaw cell containing a more viscous liquid, *Proc. R. Soc. London, Ser. A* **245**, 312 (1958).
 - [8] D. Salin and L. Talon, Revisiting the linear stability analysis and absolute-convective transition of two fluid core annular flow, *J. Fluid Mech.* **865**, 743 (2019).
 - [9] R. Govindarajan and K. C. Sahu, Instabilities in viscosity-stratified flow, *Annu. Rev. Fluid Mech.* **46**, 331 (2014).
 - [10] A. P. Hooper and W. G. C. Boyd, Shear-flow instability due to a wall and a viscosity discontinuity at the interface, *J. Fluid Mech.* **179**, 201 (1987).
 - [11] A. P. Hooper and W. G. C. Boyd, Shear-flow in stability at the interface between two viscous fluids, *J. Fluid Mech.* **128**, 507 (1983).
 - [12] F. Charru and E. J. Hinch, Phase diagram of interfacial instabilities in a two-layer Couette flow and mechanism of the long-wave instability, *J. Fluid Mech.* **414**, 195 (2000).
 - [13] E. J. Hinch, A note on the mechanism of the instability at the interface between two shearing fluids, *J. Fluid Mech.* **144**, 463 (1984).
 - [14] Y. Renardy, Instability at the interface between two shearing fluids in a channel, *Phys. Fluids* **28**, 3441 (1985).
 - [15] P. Barthelet, F. Charru, and J. Fabre, Experimental study of interfacial long waves in a two-layer shear flow, *J. Fluid Mech.* **303**, 23 (1995).

- [16] T. W. Kao and C. Park, Experimental investigations of the stability of channel flows. Part 1. Flow of a single liquid in a rectangular channel, *J. Fluid Mech.* **43**, 145 (1970).
- [17] M. E. Charles and L. U. Lilleleht, An experimental investigation of stability and interfacial waves in co-current flow of two liquids, *J. Fluid Mech.* **22**, 217 (1965).
- [18] T. G. Theofanous, R. R. Nourgaliev, and B. Khomami, An experimental/theoretical investigation of interfacial instabilities in superposed pressure-driven channel flow of Newtonian and well characterized viscoelastic fluids. Part I. Linear stability and encapsulation effects, edited by B. Khomami and C. Su. Kuan, *J. Non-Newtonian Fluid Mech.* **143**, 131 (2007).
- [19] M. Sangalli, C. T. Gallagher, D. T. Leighton, H. C. Chang, and M. J. McCready, Finite-Amplitude Waves at the Interface between Fluids with Different Viscosity: Theory and Experiments, *Phys. Rev. Lett.* **75**, 77 (1995).
- [20] I. Barmak, A. Gelfgat, H. Vitoshkin, A. Ullmann, and N. Brauner, Stability of stratified two-phase flows in horizontal channels, *Phys. Fluids* **28**, 044101 (2016).
- [21] S. G. Yiantsios and B. G. Higgins, Linear stability of plane Poiseuille flow of two superposed fluids, *Phys. Fluids* **31** 3225 (1988).
- [22] P. Guillot, A. Colin, A. S. Utada, and A. Ajdari, Stability of a Jet in Confined Pressure-Driven Biphasic Flows at Low Reynolds Numbers, *Phys. Rev. Lett.* **99**, 104502 (2007).
- [23] H. H. Hu and D. D. Joseph, Lubricated pipelining: Stability of core-annular flow. Part 2, *J. Fluid Mech.* **205**, 359 (1989).
- [24] D. T. Papageorgiou, C. Maldarelli, and D. S. Rumschitzki, Nonlinear interfacial stability of core-annular film flows, *Phys. Fluids A* **2**, 340 (1990).
- [25] A. S. Utada, A. Fernandez-Nieves, J. M. Gordillo, and D. A. Weitz, Absolute Instability of a Liquid Jet in a Coflowing Stream, *Phys. Rev. Lett.* **100**, 014502 (2008).
- [26] H. Power and M. Villegas, Weakly nonlinear instability of the flow of two immiscible liquids with different viscosities in a pipe, *Fluid Dyn. Res.* **7**, 215 (1991).
- [27] D. D. Joseph, R. Bai, and K. P. Chen, Core-annular flows, *Annu. Rev. Fluid Mech.* **29**, 65 (1997).
- [28] M. G. Blyth, H. Luo, and C. Pozrikidis, Stability of axisymmetric core-annular flow in the presence of an insoluble surfactant, *J. Fluid Mech.* **548**, 207 (2006).
- [29] G. Ooms, A. Segal, A. J. van der Wees, R. Meerhoff, and R. V. A. Oliemans, A theoretical model for core-annular flow of a very viscous oil core and a water annulus through a horizontal pipe, *Int. J. Multiphase Flow* **10**, 41 (1983).
- [30] P. T. Than, F. Rosso, and D. D. Joseph, Instability of Poiseuille flow of two immiscible liquids with different viscosities in a channel, *Int. J. Eng. Sci.* **25**, 189 (1987).
- [31] C. E. Hickox, Instability due to viscosity and density stratification in axisymmetric pipe flow, *Phys. Fluids* **14**, 251 (1971).
- [32] A. L. Frenkel and D. Halpern, Stokes-flow instability due to interfacial surfactant, *Phys. Fluids* **14**, L45 (2002).
- [33] A. P. Hooper, Long-wave instability at the interface between two viscous fluids: Thin layer effects, *Phys. Fluids* **28**, 1613 (1985).
- [34] C. S. Yih, Instability due to viscosity stratification, *J. Fluid Mech.* **27**, 337 (1967).
- [35] B. Khomami and K. C. Su, An experimental/theoretical investigation of interfacial instabilities in superposed pressure-driven channel flow of Newtonian and well characterized viscoelastic fluids Part I: Linear stability and encapsulation effects, *J. Non-Newtonian Fluid Mech.* **91**, 59 (2000).
- [36] X. Hu and T. Cubaud, From droplets to waves: Periodic instability patterns in highly viscous microfluidic flows, *J. Fluid Mech.* **887**, A27 (2020).
- [37] X. Hu and T. Cubaud, Viscous Wave Breaking and Ligament Formation in Microfluidic Systems, *Phys. Rev. Lett.* **121**, 044502 (2018).
- [38] K. S. Jayaprakash and A. K. Sen, Droplet encapsulation of particles in different regimes and sorting of particle-encapsulating-droplets from empty droplets, *Biomicrofluidics* **13**, 034108 (2019).
- [39] K. S. Jayaprakash, U. Banerjee, and A. K. Sen, Dynamics of aqueous droplets at the interface of coflowing immiscible oils in a microchannel, *Langmuir* **32**, 2136 (2016).

- [40] K. S. Jayaprakash, U. Banerjee, and A. K. Sen, Dynamics of rigid microparticles at the interface of co-flowing immiscible liquids in a microchannel, *J. Colloid Interface Sci.* **493**, 317 (2017).
- [41] B. Gol, F. J. Tovar-Lopez, M. E. Kurdzinski, S. Y. Tang, P. Petersen, A. Mitchell, and K. Khoshmanesh, Continuous transfer of liquid metal droplets across a fluid-fluid interface within an integrated microfluidic chip, *Lab Chip* **15**, 2476 (2015).
- [42] N. N. Deng, W. Wang, X. J. Ju, R. Xie, and L. Y. Chu, Spontaneous transfer of droplets across microfluidic laminar interfaces, *Lab Chip* **16**, 4326 (2016).
- [43] M. Yamada, V. Kasim, M. Nakashima, J. Edahiro, and M. Seki, Continuous cell partitioning using an aqueous two-phase flow system in microfluidic devices, *Biotechnol. Bioeng.* **88**, 489 (2004).
- [44] M. Tsukamoto, S. Taira, S. Yamamura, Y. Morita, N. Nagatani, Y. Takamura, and E. Tamiya, Cell separation by an aqueous two-phase system in a microfluidic device, *Analyst* **134**, 1994 (2009).
- [45] S. Hazra, K. S. Jayaprakash, K. Pandian, A. Raj, S. K. Mitra, and A. K. Sen, Non-inertial lift induced migration for label-free sorting of cells in a co-flowing aqueous two-phase system, *Analyst* **144**, 2574 (2019).
- [46] D. Yuan, S. H. Tan, R. Sluyter, Q. Zhao, S. Yan, N. T. Nguyen, J. Guo, J. Zhang, and W. Li, On-chip microparticle and cell washing using coflow of viscoelastic fluid and Newtonian fluid, *Anal. Chem.* **89**, 9574 (2017).
- [47] F. Tian, W. Zhang, L. Cai, S. Li, G. Hu, Y. Cong, C. Liu, T. Li, and J. Sun, Microfluidic co-flow of Newtonian and viscoelastic fluids for high-resolution separation of microparticles, *Lab Chip* **17**, 3078 (2017).
- [48] E. Hemachandran, S. Z. Hoque, T. Laurell, and A. K. Sen, Reversible Stream Drop Transition in a Microfluidic Coflow System Via on Demand Exposure to Acoustic Standing Waves, *Phys. Rev. Lett.* **127**, 134501 (2021).
- [49] B. Rallabandi, N. Oppenheimer, M. Y. Ben Zion, and H. A. Stone, Membrane-induced hydroelastic migration of a particle surfing its own wave, *Nat. Phys.* **14**, 1211 (2018).
- [50] S. M. Yang and L. G. Leal, Motions of a fluid drop near a deformable interface, *Int. J. Multiphase Flow* **16**, 597 (1990).
- [51] R. Trouilloud, T. S. Yu, A. E. Hosoi, and E. Lauga, Soft swimming: Exploiting Deformable Interfaces for Low Reynolds Number Locomotion, *Phys. Rev. Lett.* **101**, 048102 (2008).
- [52] M. Abkarian, C. Lartigue, and A. Viallat, Tank Treading and Unbinding of Deformable Vesicles in Shear Flow: Determination of the Lift Force, *Phys. Rev. Lett.* **88**, 068103 (2002).
- [53] M. Abkarian and A. Viallat, Dynamics of vesicles in a wall-bounded shear Flow, *Biophys. J.* **89**, 1055 (2005).
- [54] P. Sajeesh, M. Doble, and A. K. Sen, Hydrodynamic resistance and mobility of deformable objects in microfluidic channels, *Biomicrofluidics* **8**, 054112 (2014).
- [55] J. Carneiro, E. Doutel, J. B. L. M. Campos, and J. M. Miranda, PDMS droplet formation and characterization by hydrodynamic flow focusing technique in a PDMS square microchannel, *J. Micromech. Microeng.* **26**, 105013 (2016).
- [56] E. Chiarello, L. Derzsi, M. Pierno, G. Mistura, and E. Piccin, Generation of oil droplets in a non-Newtonian liquid using a microfluidic T-junction, *Micromachines* **6**, 1825 (2015).
- [57] S. H. Tan, N. T. Nguyen, Y. C. Chua, and T. G. Kang, Oxygen plasma treatment for reducing hydrophobicity of a sealed polydimethylsiloxane microchannel, *Biomicrofluidics* **4**, 032204 (2010).
- [58] See Supplemental Material at <http://link.aps.org/supplemental/10.1103/PhysRevFluids.7.054201> for in-depth description of velocity profiles of different fluid combinations, numerical model, variation of amplitude with droplet spacing, comparison of coefficients, and contrasting migration behavior of droplets of different β .
- [59] S. Hazra, S. K. Mitra, and A. K. Sen, Lateral migration of viscoelastic droplets in a viscoelastic confined flow: Role of discrete phase, *Soft Matter* **15**, 9003 (2019).
- [60] P. M. Bungay and H. Brenner, Pressure drop due to the motion of neutrally buoyant particles in duct flows. III. Non-neutrally buoyant spherical droplets and bubbles, *ZAMM* **53**, 187 (1973).
- [61] S. Hazra, A. Nath, S. K. Mitra, and A. K. Sen, Dynamics of rigid particles in a confined flow of viscoelastic and strongly shear-thinning fluid at very small Reynolds numbers, *Phys. Fluids* **33**, 052001 (2021).